Journal of Materials Chemistry B

ROYAL SOCIETY OF CHEMISTRY

PAPER

View Article Online
View Journal | View Issue

Cite this: J. Mater. Chem. B, 2022, 10, 9848

A water-soluble thiophene-croconaine dye with a high molar extinction coefficient for NIR fluorescence imaging-guided synergistic photothermal/photodynamic therapy of cancer†

E Pang,‡[a] Rong Huang,‡[a] Shaojing Zhao,[a] Ke Yang,[a] Baoling Li,[a] Qiuxia Tan,[a] Siyi Tan,[b] Minhuan Lan,*[a] Benhua Wang*[a] and Xiangzhi Song*[a]

Received 19th August 2022,
Accepted 8th November 2022

DOI: 10.1039/d2tb01772e

rsc.li/materials-b

Phototherapeutic agents with near-infrared (NIR) fluorescence, strong reactive oxygen species generation and photothermal conversion capabilities are highly desirable for use in cancer therapy. Herein, a water-soluble NIR croconaine dye (**TCR**) with a thiophene-croconaine rigid core and two symmetric alkyl chains was designed and synthesized. **TCR** exhibits intense NIR absorption and fluorescence that peaked at 780 and 815 nm, respectively, with a high molar extinction coefficient of 1.19×10^5 M^{-1} cm^{-1}. Moreover, **TCR** has a high photothermal conversion efficiency of 77% and is capable of generating hydroxyl radicals ($OH^{\bullet}$) under 735 nm laser irradiation. Based on these outstanding properties, **TCR** has proven its application in NIR fluorescence imaging-guided synergistic photothermal/photodynamic therapy of cancer.

Introduction

Phototherapy, such as photodynamic therapy (PDT) and photothermal therapy (PTT), has the advantages of non-invasiveness, high selectivity, negligible drug resistance and low toxic side effects.[1,2] Unfortunately, the limitations of single treatment are becoming increasingly apparent, *i.e.*, the hypoxic microenvironment of tumor reduces the efficacy of oxygen-dependent PDT, whereas the rapid heating of PTT can evoke a heat shock immune response and increase the thermotolerance of tumor cells.[3,4] Therefore, the combination of PTT and PDT is undoubtedly the desired choice for achieving ideal therapeutic outcomes.[5]

Imaging-guided phototherapy can realize accurate cancer diagnosis, thereby improving the selectivity in cancer treatment.[6] Various phototheranostics integrating fluorescence imaging and therapeutic functions have been reported.[7] Some reported fluorescent inorganic nanomaterials can generate reactive oxygen species (ROS) and heat under laser excitation.[8] However, their clinical use is limited due to the issues of non-degradation, poor biocompatibility, low ROS generation or photothermal conversion efficiency (PCE).[9] Organic photosensitizers, including porphyrins, hypocrellins, and phthalocyanines, exhibit deep red fluorescence, high singlet oxygen quantum yield, and acceptable biodegradation and have been approved for clinical use.[10] However, most of them have the following drawbacks: (i) poor water solubility and easy aggregation in living systems; (ii) weak photothermal effects due to a low PCE; and (iii) short excitation and emission wavelengths. More importantly, their molar absorption coefficient in a phototherapeutic window (650–900 nm) is low (Table S1, ESI†).[11–13] Hence, developing efficient phototheranostics with good water solubility, high ROS generation and PCE, and strong absorption/emission in the therapeutic window is highly desirable.

Croconium (CR) dyes have strong absorption in the NIR region with a really high molar absorption coefficient ($\sim 10^5$ M^{-1} cm^{-1}).[14,15] Because of their excellent photobleaching resistance, thermal stability and spectral tunability, the CR dyes have been widely used in biomedical sensing, PTT, and photoacoustic imaging.[16] Smith *et al.* prepared a pH-responsive CR dye with a high PCE for ratiometric photoacoustic imaging by trapping the CR dye in a tetralactam macrocycle.[17] Li *et al.* synthesized shape-controlled CR-based A1094@DSPE-PEG2000 micelles, which have absorption in the NIR-II region and show good photothermal conversion and photoacoustic imaging capabilities.[18] Chen *et al.* assembled CR dyes with human serum albumin *via* hydrophobic interaction to form stable nanoparticles for photoacoustic imaging.[19]

[a] Hunan Provincial Key Laboratory of Micro & Nano Materials Interface Science, College of Chemistry and Chemical Engineering, Central South University, Changsha, P. R. China. E-mail: minhuanlan@csu.edu.cn, benhuawang@csu.edu.cn, xzsong@csu.edu.cn

[b] Huazhi medical laboratory Co., Ltd, 618 Heping Road, Changsha, 410125, P. R. China

† Electronic supplementary information (ESI) available. See DOI: https://doi.org/10.1039/d2tb01772e

‡ These authors contributed equally to this work.

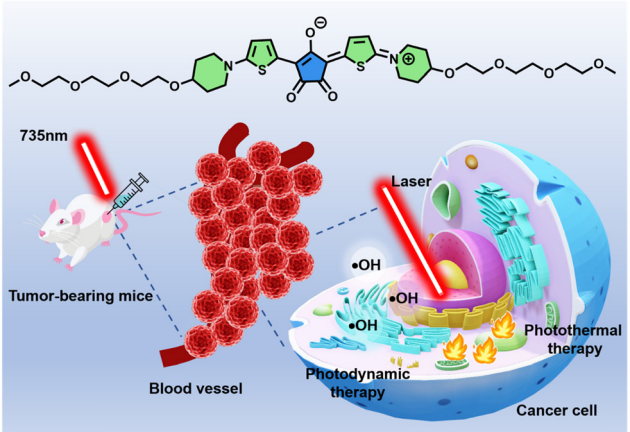

Scheme 1 Molecular structure of TCR and its application in photothermal and photodynamic therapy of cancer.

However, most of the previous CR dyes were assembled with foreign water-soluble materials. Although some CR dyes exhibited good photothermal conversion capability, no examples were reported in ROS generation. Herein, we designed and synthesized a new CR dye (**TCR**) using aminothiophene as the donor, which contained a triethylene glycol chain to improve the water solubility (Scheme 1). Aqueous **TCR** solution possesses strong NIR absorption and fluorescence that peaked at 780 and 815 nm, respectively. Remarkably, **TCR** has a high PCE of 77%, and is capable of generating $OH^{\bullet}$ under 735 nm laser irradiation. The heat and $OH^{\bullet}$ could effectively terminate DNA replication, force the cytoskeleton to collapse, inhibit proliferation and enable ablation of tumor cells. Herein, the application of **TCR** in NIR fluorescence imaging-guided photothermal/photodynamic therapy of cancer was firstly demonstrated.

Experimental

Materials

4-Hydroxypiperidinehydrochloride, tosyl chloride, thienyl mercaptan and croconaine were purchased from Wuhan Changsheng Huacheng Technology Development Co., Ltd. Di-*tert*-butyl dicarbonate, TEA, triethylene glycol monoethyl ether, NaOH, NaH, and trifluoroacetic acid were purchased from Titan Technology Co., Ltd, and indocyanine green (ICG) and terephthalic acid (TA) were purchased from Energy Chemical. YF®Click-iT EdU was purchased from Shanghai Biosai Biotechnology Co., Ltd. 2′,7′-Dichlorofluorescein diacetate (DCFH-DA) was purchased from McLean Biochemical Technology Co., Ltd. The Annexin V-FITC/7-AAD Apoptosis Assay Kit was purchased from Melan Biologicals Co., Ltd. Calcein acetoxymethylester (calcein AM), propidium iodide (PI) and 3-(4,5-dimethylthiazol-2-yl)-2,5-diphenyltetrazolium bromide (MTT) were purchased from Tianjin Heans Biochemical Technology Co., Ltd.

Instruments

^{1}H-NMR and ^{13}C-NMR spectra were collected on a Bruker Advance-400 spectrometer with tetramethylsilane (TMS) as the internal standard. Matrix-assisted laser desorption ionization-time-of-flight (MALDI-TOF) mass spectra were obtained on a Bruker Microflex mass spectrometer. The UV-vis absorption and fluorescence spectra were recorded on Shimadzu UV2600 and RF6000 spectrophotometers, respectively.

MTT experiments

4T1 cells were seeded in 96-well plates. After 24 h incubation, **TCR** at different concentrations (1.2, 2.4, 4.8, 7.2 and 9.6 μM) was added and incubated for another 4 h, and then the cells were exposed to laser irradiation for 10 min (735 nm, 1.0 W cm^{-2}) for the phototoxicity study. For the dark toxicity, cells were incubated with different concentrations of **TCR** for 24 h. The cell viability was calculated according to the standard MTT protocols.

FITC-labeled phalloidin experiment

4T1 cells were seeded in four confocal discs that were named PBS, PBS + laser, **TCR** and **TCR** + laser groups. After 24 h, the medium was discarded and then **TCR** (9.6 μM) was added to two of the confocal discs (**TCR** and **TCR** + laser groups), incubated for another 4 h. Then the PBS + laser and **TCR** + laser groups were irradiated with a 735 nm laser (1.0 W cm^{-2} for 10 min). After laser irradiation, the cells were gently washed twice with PBS. Subsequently, each group of cells was treated with 200 μL of FITC-labeled phalloidin and incubated for 30 min at room temperature (note: light-protection is required). The cells were washed twice again with PBS before imaging using confocal laser scanning microscopy (CLSM).

EdU cell proliferation experiment

4T1 cells were divided into four groups: PBS, PBS + laser, **TCR** and **TCR** + laser groups and evenly planted in 96-well plates. After 24 h, the culture media of **TCR** and **TCR** + laser groups were replaced with fresh DMEM media containing **TCR** and incubated for 4 h. Subsequently, the PBS + laser and **TCR** + laser groups were illuminated with a 735 nm laser (1 W cm^{-2}, 10 min). After illumination, the culture medium of each group of cells was washed with PBS three times. Then, the cells were fixed with 4% polyformaldehyde. After 30 min, the cells were washed with PBS three times, and 50 μL glycine (2 mg mL^{-1}) was added into each well to neutralize excess aldehyde groups. After 5 min, each well was treated with YF488® for 30 min. Then, 100 μL of Hoechst 33342 solution was added to each well, incubated at room temperature and protected from light for 15–30 min and the Hoechst 33342 solution was removed and washed twice with 100 μL PBS for imaging.

Annexin V/7-AAD flow cytometry

An Annexin V-FITC/7-AAD Apoptosis Assay Kit was used to analyze the apoptosis of the cells. Specifically, 4T1 cells were seeded in 24-well plates. After the cells adhere to the 24-well plates, PBS or **TCR** solution was added to the cells of the different groups and incucated for 4 h, followed by treatment with or without laser (735 nm, 1.0 W cm^{-2}). All cells obtained in the 24-well plates were collected (to avoid experimental errors, cells that had died in the medium needed to be collected), and

after centrifugation, 500 μl of diluted working solution and 5 μl of FITC and 7-AAD were added to each group of cells and tested immediately.

Animal model

The mice used for fluorescence imaging and cancer treatment were purchased from Hunan Slaughter Jingda Laboratory Animal Co., Ltd. All relevant animal experiments were performed in accordance with the guidelines approved by the Ethics Committee of Central South University (No. 430727211101478756). 4T1 cells were injected into the right back of mice (BALB/c, male, 8 weeks) to construct a 4T1 tumor-bearing mouse model. When the tumor volume grew to about ~150 mm^3, animal experiments were started.

In vivo fluorescence imaging

Aqueous **TCR** solution (200 μL, 9.6 μM) was injected intratumorally into 4T1 tumor-bearing mice, followed by fluorescence imaging using the animal imaging system IVIS Lumina XR (λ_{ex} = 640 nm, λ_{em} = 710 nm).

In vivo cancer therapy

Mice were first anesthetized (10% chloral hydrate, 60 μL), and then intratumorally injected with PBS (200 μL) or **TCR** (9.6 μM, 200 μL) and treated with laser irradiation (735 nm, 1 W cm^{-2}, 10 min) or no irradiation. For the next 14 days, the tumor volumes of the mice were recorded every 2 days using vernier calipers, and the weights of the mice were recorded using a weighing scale.

Calculation of mass extinction coefficients

According to the Beer–Lambert Law (eqn (1)), the mass extinction coefficient (ε) of **TCR** was calculated using the following formula:

$$A = \varepsilon \times b \times c \quad (1)$$

where A represents the absorbance, b represents the thickness of the fluorescence cell (determined as 1 cm), and c represents the mass concentration. An accurate amount of **TCR** was weighed and then tested for the UV-visible absorption spectrum after diluting it to a lower concentration with ultrapure water. The mass extinction coefficient and molar extinction coefficient of TCR were calculated to be 154.95 g^{-1} L cm^{-1} and 1.19 × 10^5 M^{-1} cm^{-1}, respectively.

Calculation of photothermal conversion efficiency (η):

η was calculated according to eqn (2):

$$\eta = \frac{hA(T_{Max} - T_{Surr}) - Q_{Dis}}{I(1 - 10^{-A_{808}})} \quad (2)$$

where T_{Max} and T_{Surr} are the plateau and surrounding temperature, respectively. Q_{Dis} represents the resulting heat dissipation due to the solvent and I is the laser power intensity. hA was obtained from eqn (3):

$$\tau = \frac{m_D c_D}{hA} \quad (3)$$

where m_D and c_D are the mass and heat capacity of DI water, respectively. τ_s was calculated using eqn (4):

$$t = -\tau_s \ln(\theta) = -\tau_s \ln\left(\frac{T_l - T_{Surr}}{T_{Max} - T_{surr}}\right) \quad (4)$$

where t is the cooling time point after continuous irradiation for 10 min and T_t is the corresponding temperature. Q_D is determined according to eqn (5):

$$Q_{Dis} = \frac{C_D m_D (T_{Max(water)} - T_{Surr})}{\tau_{S(water)}} \quad (5)$$

According to the experimental data and the above equations, η was calculated to be 77%.

Results and discussion

Fig. 1a shows the chemical structure of **TCR**, in which, a triethylene glycol chain was introduced to improve the water solubility. The detailed synthesis and characterization of **TCR** are described in Scheme S1 and Fig. S1–S12 (ESI†). The optimized geometries of the ground state of **TCR** exhibited a large overlap of the HOMO and LUMO (Fig. 1b), enabling **TCR** to possess an efficient intramolecular charge transfer from thiophene to crotonic acid.[20] As expected, aqueous **TCR** solution exhibited strong NIR absorption and fluorescence that peaked at 780 and 815 nm, respectively, with a high molar extinction coefficient of 1.19 × 10^5 M^{-1} cm^{-1} (Fig. 1c). The scanning electron microscopy (SEM) image and the corresponding size histogram of **TCR** show an average diameter of approximately 36 nm (Fig. 1d and Fig. S13, ESI†), indicating its homogeneity and good water dispersion.

The photothermal conversion capability of **TCR** was investigated by using a 735 nm laser. As shown in Fig. 2a and b, the temperature changes of **TCR** showed dependence on concentration and laser power, *i.e.*, under a laser power of 1.0 W cm^{-2}, the temperature of **TCR** solution (9.6 μM) rapidly increased to

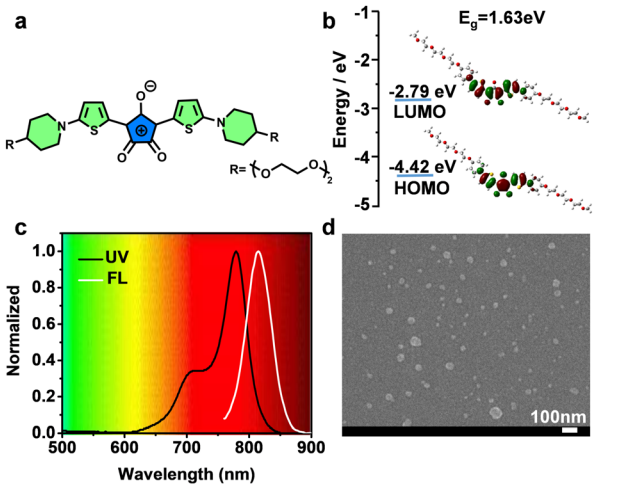

Fig. 1 Chemical structure (a) and molecular frontier orbitals of the ground state (b) of **TCR**. (c) Normalized UV-vis absorption and fluorescence spectra of **TCR**. (d) SEM image of **TCR** nanoparticles, scale bar: 100 nm.

67 °C within 10 min, which was sufficient to trigger cancer cell death. In addition, the corresponding infrared thermal images shown in Fig. 2c further confirmed the outstanding photothermal conversion ability of **TCR**. The PCE of **TCR** at 735 nm was calculated to be 77%, which exceeded those of most of the reported CR dyes (Table S2, ESI†).[21,22] Moreover, **TCR** also exhibited superior photostability. As shown in Fig. 2d, after 6 cycles of laser irradiation for 10 min and cooling down to the initial temperature, the heating rate of **TCR** remained constant, while indocyanine green (ICG) had decomposed substantially.

Then the ROS-generating capacity of **TCR** was investigated by using 9,10-anthracenediyl-bis(methylene) dimalonic acid (ABDA) and terephthalic acid (TA) to capture the singlet oxygen and $OH^{\bullet}$, respectively. As revealed in Fig. 2e, no obvious absorbance reduction was observed in **TCR**-ABDA mixed solution when exposed to 735 nm laser irradiation. In contrast, the fluorescence intensity of **TCR**-TA mixed solution gradually increased with prolonged irradiation time (Fig. 2f), while in the absence of **TCR**, the fluorescence of aqueous TA solution showed no obvious variations (Fig. S14, ESI†). The above results suggested that **TCR** could generate $OH^{\bullet}$ under laser irradiation. Interestingly, this is the first example to show that CR dyes could generate $OH^{\bullet}$.

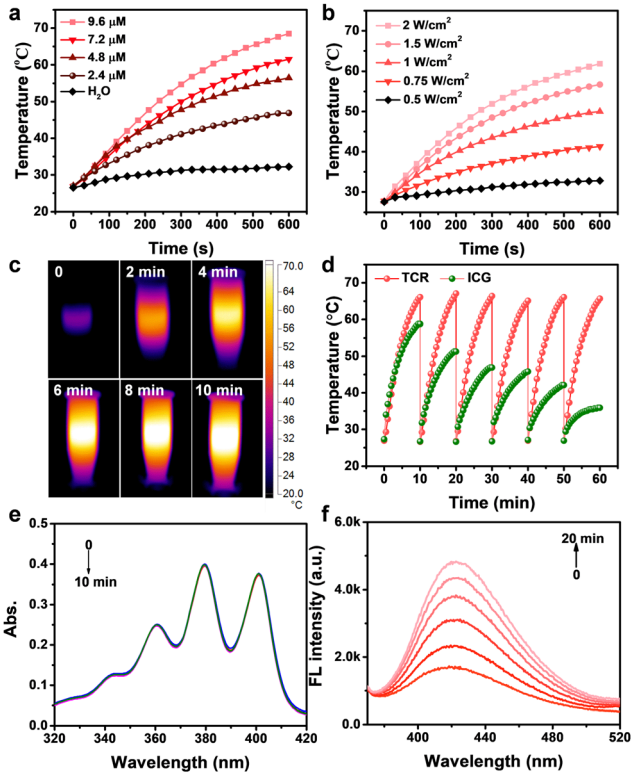

Fig. 2 (a) Concentration- and (b) laser power-dependent temperature changes of **TCR**. (c) Thermal infrared images of aqueous **TCR** solution at different irradiation times. (d) Temperature elevation by **TCR** (9.6 μM) and ICG (9.6 μM) for 6 cycles of irradiation (735 nm, 1.0 W cm^{-2}). (e) UV-vis absorption spectra of the **TCR**–ABDA mixture under laser irradiation (735 nm, 1.0 W cm^{-2}). (f) Time-dependent fluorescence spectral changes of the **TCR**–TA mixture under laser irradiation (λ_{ex} = 320 nm, 1.0 W cm^{-2}).

The $OH^{\bullet}$ generation of **TCR** was further investigated by using 2′,7′-dichlorodihydrofluorescein diacetate (DCFH-DA) as an ROS trapper, which emits green fluorescence upon reacting with ROS.[23] As shown in Fig. 3a, green fluorescence was obviously detected in cells of the **TCR** + laser group, while no fluorescence signal was observed in the other three groups, confirming the ability of **TCR** to efficiently produce $OH^{\bullet}$ under laser irradiation. Considering the high PCE and excellent $OH^{\bullet}$ generation capability, the phototheranostic properties of **TCR** were further studied. As shown in Fig. 3b, the cell viability of 4T1 cells incubated with **TCR** or **TCR** + Vitamin C (Vc) under dark conditions exceeded 95%, even at a high concentration of 9.6 μM. In contrast, the cell viability in the **TCR** + laser group exhibited dependence on the **TCR** concentration, with a sharp decrease after 10 min of laser irradiation. The half-maximal inhibitory concentration (IC_{50}) was calculated to be ~4.8 μM. These results reveal that **TCR** has excellent biocompatibility and high phototoxicity. To further verify the photodynamic activity of **TCR**, 4T1 cells were co-incubated with **TCR** and Vc and then exposed to laser irradiation. Interestingly, the cell viability of the **TCR** + Vc + laser group was higher than that of the **TCR** + laser group, suggesting that $OH^{\bullet}$ produced by the excited **TCR** was also effective in killing cancer cells. Similarly, TCR also exhibits phototoxicity to normal cells (HUEVC) (Fig. S15, ESI†).

The phototherapeutic effect of **TCR** on 4T1 cells was further investigated by using calcein-AM and propidium iodide (PI) as staining dyes for the live and dead cells, respectively.[24] As shown in Fig. 3c, cells were incubated with **TCR** followed by laser treatment emitted strong red fluorescence, while cells from the other three control groups emitted green fluorescence, indicating that **TCR** had little effect on the activity of cells, and

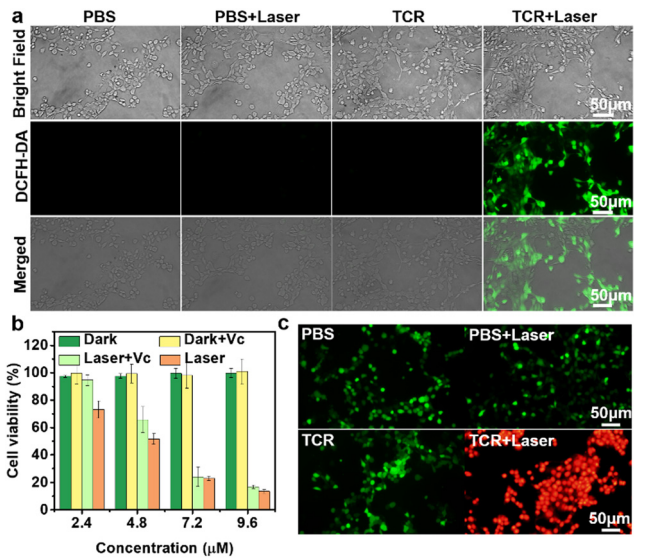

Fig. 3 (a) Images of 4T1 cells incubated with DCFH-DA from different groups. (b) Cytotoxicity assays of **TCR** against 4T1 tumor cells with different treatments (**TCR**, **TCR** + V_C, **TCR** + V_C + laser, and **TCR** + laser). (c) Images of 4T1 cells incubated with calcein-AM and PI from different groups (735 nm, 1.0 W cm^{-2}, 10 min).

that 735 nm laser-treated **TCR** was effective in killing cancer cells. To further understand the mechanism of cell death, flow cytometry assay was carried out to analyze apoptotic and necrotic cells.[25] As shown in Fig. 4a, in the absence of laser irradiation or **TCR**, no significant early apoptosis, late apoptosis or necrosis was observed. However, after exposure to NIR laser irradiation, **TCR** induced 27.80% of the early apoptotic cells and 66.25% of the later apoptotic/necrotic cells, while the control group maintained a high cell viability. The above results demonstrated that **TCR** could induce apoptosis or necrosis of tumor cells by producing efficient photothermal effects and $OH^{\bullet}$.

Considering the significance of cancer cytoskeletal junctions for migration, the changes of the cytoskeleton after different treatments were subsequently explored. FITC-labeled phalloidin was used to label filamentous actin (F-actin) in 4T1 cells.[26] As shown in Fig. 4b, the cytoskeleton of 4T1 cells in the three control groups still showed a homogenous and well-distributed morphology, however, the **TCR** + laser group showed obvious fragments of filamentous cell structures, indicating that the cytoskeletal filaments collapsed after **TCR** + laser treatment. Therefore, visualization of the cell death process proved the phototherapeutic effect of **TCR**. Cell proliferation is the basis for living organisms' growth, development, reproduction, and inheritance. 5-Ethynyl-2′-deoxyuridine (EdU) is a pyrimidine analogue that is incorporated into the DNA double-strand during DNA synthesis. The specific reaction between EdU and fluorescent dye YF488® can generate green fluorescence.[27] To demonstrate **TCR**'s ability to inhibit cancer cell growth under laser irradiation, the cells' proliferative status was examined. As shown in Fig. 4c, PBS and **TCR** treated groups had no significant effect on cell proliferation in the absence of laser irradiation, while no green fluorescence signal was observed in the **TCR** + laser group, indicating that **TCR** effectively interrupted cell proliferation by inhibiting DNA synthesis.

Next, we evaluated the performance of **TCR**-guided phototherapeutics by *in vivo* imaging of tumor-bearing mice. As shown in Fig. 5a, no fluorescence was observed after intratumoral injection of PBS. In contrast, an intense red fluorescence signal was detected in the tumor region after intratumoral injection of **TCR** solution. Guided by the intense NIR fluorescence imaging, the treatment was conducted on 4T1 tumor-bearing mice. As shown in Fig. 5b and Fig. S16 (ESI†), the temperature of the tumor site did not change in the absence of laser irradiation, and there was only a slight increase in the temperature of the tumor site after injection of PBS under laser irradiation. In contrast, after injection of **TCR** solution, the temperature of the tumor site gradually increased as the laser irradiation time increased, and after 10 minutes, the temperature of the tumor site was close to 70 °C, which was sufficient to effectively ablate the tumor cells. In addition, the ability of **TCR** to inhibit tumor growth was investigated. 4T1 tumor-bearing mice were randomly divided into four groups: (1) PBS, (2) PBS + laser,

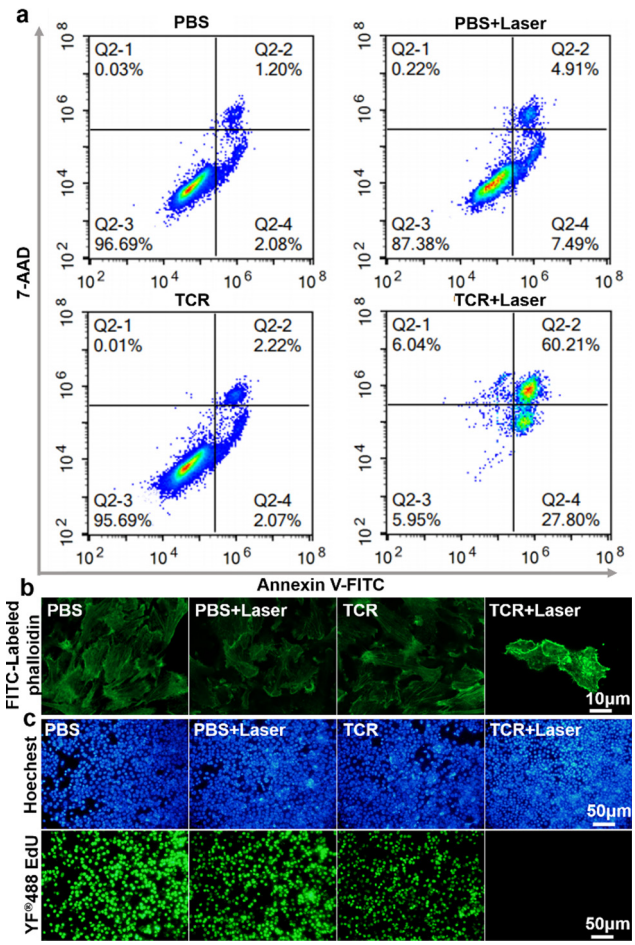

Fig. 4 (a) Flow cytometry analysis of 4T1 cells of different experimental groups. Confocal fluorescence images of (b) phalloidin-labeled and (c) EdU stained 4T1 cells of different experimental groups.

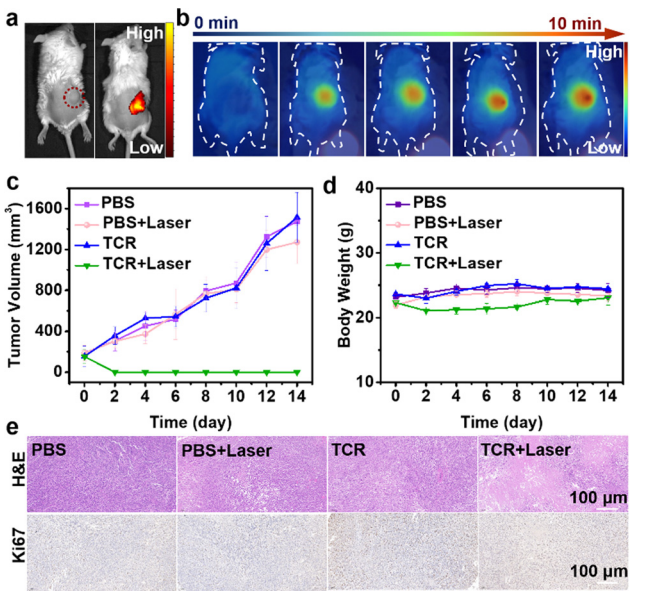

Fig. 5 (a) Fluorescence images of tumor-bearing mice after injecting PBS (left) and **TCR** (right). (b) Infrared thermal images of tumor-bearing mice after **TCR** injection under laser irradiation. Tumor sizes (c), body weights (d) and images of tumor sections (e) after different treatments (scale bar: 100 μm).

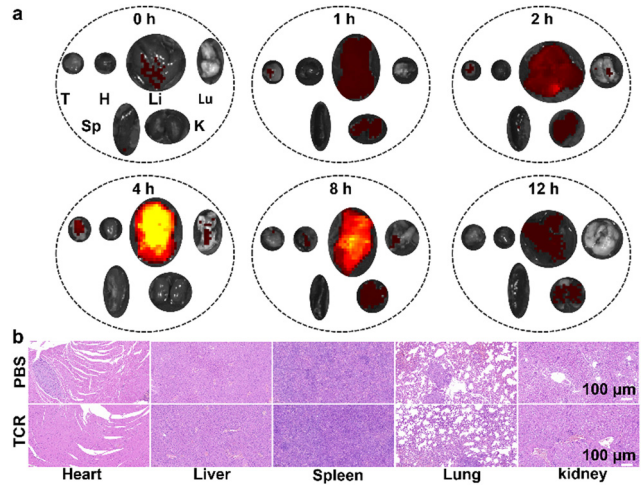

Fig. 6 (a) Fluorescence images of major organs, including heart (H), liver (Li), lungs (Lu), spleen (Sp), kidneys (K) and tumor (T) of mice after intravenous TCR injection. (b) Images of H&E and Ki67 stained sections of organs from mice in the PBS and TCR groups.

(3) **TCR**, and (4) **TCR** + laser. As shown in Fig. 5c, tumors in groups 1–3 grew rapidly and malignantly, indicating that PBS only, PBS + laser, or **TCR** only had negligible effects on tumor growth. The **TCR** + laser group, however, effectively inhibited the tumor growth with no significant recurrence in the following 14 days, demonstrating the excellent therapeutic effect of **TCR** on tumors. In addition, no obvious weight change was observed in the corresponding groups, implying negligible toxicity of **TCR** on the mice (Fig. 5d). To verify the proliferation inhibition effect of **TCR** on tumors, tumor sections were evaluated.[28] Hematoxylin and eosin (H&E) and Ki67 staining of tumor sections showed that **TCR** induced more areas of necrosis and significantly inhibited tumor proliferation after laser irradiation (Fig. 5e).

Based on the excellent performance of **TCR**, we further investigated the *in vivo* physiological safety of **TCR** by quantitative fluorescence analysis of the *in vivo* metabolic processes in major organs (*i.e.*, heart, liver, spleen, lungs, and kidneys) and tumor of 4T1 tumor-bearing mice. After intravenous injection of **TCR** (200 μL, 9.6 μM) into 4T1 tumor-bearing mice, the major organs of the mice were excised at different time points (0, 1, 2, 4, 8 and 12 h). As shown in Fig. 6a and Fig. S17 (ESI†), strong NIR fluorescence was observed in the liver and kidneys after 1 h, with a maximum intensity in the liver after 4 h. Clearance and metabolism of **TCR** from the liver and kidneys were observed at the 12th h, demonstrating that the metabolic pathway of **TCR** was primarily through the liver, with the kidneys serving as a secondary metabolic modality. Furthermore, histological evaluation showed no damage to the major organs of mice after the **TCR** treatment, indicating its excellent safety (Fig. 6b). Moreover, blood tests for liver and kidney functions are shown in Table S3 (ESI†). No statistically significant difference was found in all 10 markers between mice treated with saline and **TCR**, verifying the good biocompatibility of **TCR**.

Conclusions

In summary, we designed and synthesized NIR water-soluble phototherapeutics (**TCR**) for fluorescence imaging-guided synergistic photothermal/photodynamic cancer therapy. **TCR** has a high molar extinction coefficient based on a large conjugated and symmetric D–A–D structure. In addition, **TCR** possesses good photostability, high PCE (77%), good biocompatibility, and rapid metabolism. Moreover, we demonstrated that **TCR** can ablate tumour cells by terminating DNA replication through efficient photothermal and large amounts of $OH^{\bullet}$, forcing the cytoskeleton to collapse, inhibiting cell proliferation, and achieving ablation of tumor cells. Meanwhile, **TCR** has superior biocompatibility and can be metabolized by liver and kidneys. This work provides a novel design for excellent phototherapeutics.

Author contributions

E Pang and R. Huang contributed equally to this work. M. Lan planned and supervised the project. E Pang wrote the whole manuscript. K. Yang, B. Li and Q. Tan contributed to the cell and animal experiments. S. Zhao, S. Tan, B. Wang and X. Song contributed to data analysis and polishing the article.

Conflicts of interest

The authors declare no conflicts of interest.

Acknowledgements

This work was supported by the National Natural Science Foundation of China (No. 62175262, 21907110 and 22178395), the Science and Technology Innonation Program of Hunan Province (2022RC1201) and the Fundamental Research Funds for the Central Universities of Central South University (No. 2020CX021, 2021zzts0556 and 2021zzts0521).

References

1 M. H. Lan, S. J. Zhao, W. M. Liu, C. S. Lee, W. J. Zhang and P. F. Wang, *Adv. Healthcare Mater.*, 2019, **8**, 1900132.
2 H. Y. Liu, C. Lua, L. B. Han, X. B. Zhang and G. S. Song, *Coord. Chem. Rev.*, 2021, **441**, 213978.
3 M. Qiu, Y. H. Duo, W. Y. Liang, Y. L. Yang, B. Zhang, Z. J. Xie, X. L. Yang, G. Q. Wang, N. Xie, G. H. Nie, O. A. Alhartomy, A. A. ALGhamdi, S. Wageh, Y. H. Cao and H. Zhang, *Adv. Funct. Mater.*, 2021, **31**, 2104607.
4 R. Q. Zhu, T. Q. Lang, W. L. Yan, X. Zhu, X. Huang, Q. Yin and Y. P. Li, *Adv. Sci.*, 2021, **8**, 2003542.
5 Y. F. Zhang, Y. Y. Liao, Q. N. Tang, J. Lin and P. Huang, *Angew. Chem., Int. Ed.*, 2021, **60**, 10647–10653.
6 Q. You, K. Y. Zhang, J. Y. Liu, C. L. Liu, H. Y. Wang, M. T. Wang, S. Y. Ye, H. Q. Gao, L. T. Lv, C. Wang, L. Zhu and Y. L. Yang, *Adv. Sci.*, 2020, **7**, 1903341.

7 X. M. Cheng, J. Gao, Y. Ding, Y. Lu, Q. C. Wei, D. Z. Cui, J. L. Fan, X. M. Li, E. S. Zhu, Y. N. Lu, Q. Wu, L. Li and W. Huang, *Adv. Sci.*, 2021, **8**, 2100876.
8 M. M. He, G. L. He, P. Y. Wang, S. H. Jiang, Z. Y. Jiao, D. M. Xi, P. C. Miao, X. F. Leng, Z. Y. Wei, Y. Li, Y. J. Yang, R. Wang, J. J. Du, J. L. Fan, W. Sun and X. J. Peng, *Adv. Sci.*, 2021, **8**, 2103334.
9 K. K. Wen, L. F. Wu, X. X. Wu, Y. Lu, T. Duan, H. Ma, A. D. Peng, Q. Q. Shi and H. Huang, *Angew. Chem., Int. Ed.*, 2020, **59**, 12756–12761.
10 G. T. Spence, G. V. Hartland and B. D. Smith, *Chem. Sci.*, 2013, **4**, 4240–4244.
11 B. Guo, G. X. Feng, P. N. Manghnani, X. L. Cai, J. Liu, W. B. Wu, S. D. Xu, X. M. Cheng, C. Teh and B. Liu, *Small*, 2016, **12**, 6243–6254.
12 Y. Ding, W. M. Liu, J. S. Wu, X. L. Zheng, J. C. Ge, H. L. Ren, W. J. Zhang, C. S. Lee and P. F. Wang, *Chem. – Asian J.*, 2020, **15**, 3462–3468.
13 F. Zhang, S. R. Wang, X. G. Li, Y. Xiao and J. J. Guo, *J. Mol. Struct.*, 2016, **1107**, 329–336.
14 B. L. Li, S. J. Zhao, L. Huang, Q. Wang, J. F. Xiao and M. H. Lan, *Chem. Eng. J.*, 2021, **408**, 127245.
15 B. Lu, Z. C. Zhang, D. N. Jin, X. L. Yuan, J. Wang, Y. Ding, Y. Wang and Y. Yao, *Chem. Commun.*, 2021, **57**, 12020–12023.
16 H. Q. Cao, Y. Yang, M. H. Liang, Y. T. Ma, N. Sun, X. B. Gao and J. B. Li, *Chem. Commun.*, 2021, **57**, 255–258.
17 S. Lei, Y. F. Zhang, N. T. Blum, P. Huang and J. Lin, *Bioconjugate Chem.*, 2020, **31**, 2072–2084.
18 S. Guha, G. K. Shaw, T. M. Mitcham, R. R. Bouchard and B. D. Smith, *Chem. Commun.*, 2016, **52**, 120–123.
19 H. H. Liu, X. Y. Wang, Y. F. Huang, H. H. Li, C. Y. Peng, H. Z. Yang, J. D. Li, H. W. Hong, Z. Lei, X. F. Zhang and Z. J. Li, *ACS Appl. Mater. Interfaces*, 2019, **11**, 30511–30517.
20 Q. Chen, X. D. Liu, J. F. Zeng, Z. P. Cheng and Z. Liu, *Biomaterials*, 2016, **98**, 23–30.
21 L. G. Tang, F. W. Zhang, F. Yu, W. J. Sun, M. L. Song, X. Y. Chen, X. Z. Zhang and X. L. Sun, *Biomaterials*, 2017, **129**, 28–36.
22 S. Y. Li, K. Lui, X. Li, X. Y. Fang, W. Lo, Y. J. Gu and W. T. Wong, *ACS Appl. Bio. Mater.*, 2021, **4**, 4152–4164.
23 L. N. Wang, Y. Y. Huang, Y. J. Yu, H. F. Zhong, H. H. Xiao, G. X. Zhang and D. Q. Zhang, *Adv. Healthcare Mater.*, 2021, **10**, 2100896.
24 F. T. Zeng, L. G. Tang, Q. Y. Zhang, C. R. Shi, Z. C. Huang, S. Nijiati, X. Y. Chen and Z. J. Zhou, *Angew. Chem., Int. Ed.*, 2022, **61**, e202112925.
25 F. R. Zhang, X. L. Han, Y. Y. Hu, S. H. Wang, S. Liu, X. T. Pan, H. Y. Wang, J. J. Ma, W. W. Wang, S. S. Li, Q. Y. Wu, H. Y. Shen, X. L. Yu, Q. P. Yuan and H. Y. Liu, *Adv. Sci.*, 2019, **6**, 1801507.
26 Z. Q. Guo, H. He, Y. Zhang, J. M. Rao, T. Yang, T. Li, L. Wang, M. K. Shi, M. Y. Wang, S. H. Qiu, X. Song, H. T. Ke and H. B. Chen, *Adv. Mater.*, 2021, **33**, 2004225.
27 Y. W. Bao, X. W. Hua, X. K. Chen and F. G. Wu, *Biomaterials*, 2018, **183**, 30–42.
28 C. Xu and K. Y. Pu, *Chem. Soc. Rev.*, 2021, **50**, 1111–1137.

